Pub ID 198255

Safeguards Technology Development Program
FY2023 Mid-Year Report
June 2023

WBS # – Project Title: 24.1.3.1—NDA Tech: Multimodal Data Fusion with 3D Gamma-Ray Imaging for Safeguards

HQ Team Lead and PM: Arden Dougan and James Garner]

Summary Statement of Work: Improve the quantitative results obtained from 3D gamma-ray imagers for use in safeguards inspections.

FY23: Continue to improve the numerical and 3D results obtained with gamma-ray imagers and consolidate the various algorithms for transfer to H3D, Inc.

Report Title: 2023 Mid-Year Report: Multimodal Data Fusion with 3D Gamma-Ray Imaging for Safeguards

Names of Authors and Affiliations:

Oak Ridge National Laboratory: Klaus Ziock, Alex Laminack, Jake Daughhetee, Kyle Schmitt

H3D Inc.: Willie Kaye

Major Highlights:

- A paper on the project and overall concepts was presented at the 2022 IAEA International Safeguards Symposium.
- We met with IAEA officials to discuss their vision for using the H420 in on-site inspections, providing guidance for the project goals.
- Portions of the work were presented at the annual IEEE Nuclear Science Symposium.
- The 3D MLEM projection of coded-aperture data has been used with the systematic 3D data collected late last year to demonstrate the ability to create early fusion 3D images.
- We have successfully demonstrated the ability to obtain 3D MLEM coded-aperture images that are limited to surface voxels.
- We have received and collected data with a monolithic metal mask. This non-potted mask has improved efficiency at low energies yielding an ~ 8% improvement in sensitivity at 122 keV.
- We continue to improve our characterization of the CZT detector, obtaining local-response matrices at low event rates using fine multi-slit collimators.

Progress:

Overall, progress on the project has been impacted by the staffing situation at LBNL. As indicated in the Project Work Plan (PWP), this has led to a revised schedule that includes a 6-month-long hiatus on implementation of contextual data segmentation and further Compton developments. During that time, the project has focused on improving the simulation results and the projection of coded-aperture data onto 3D scene data using the maximum likelihood expectation maximization (MLEM) algorithm [1]—

work that was started late in the previous fiscal year. We have also started to explore the software framework that will be implemented by our commercial partner, H3D, Inc.

Software Framework Development

The ultimate project goal is to improve quantitative results obtained by the IAEA with the H420 gamma-ray imager. Distribution to the IAEA will be through incorporation of project results into the software provided with the device by our commercial partner, H3D, Inc. Toward achieving that goal, we have started discussions with H3D to identify the requisite software components and how they will mesh with their own internally developed contextual data systems and other extant software components. We have identified the coded-aperture response data cube as a key structure. Discussions on contextual imaging were informative but somewhat inconclusive as the project lead on contextual data (LBNL) has not been available.

Continued Development of Quantitative 3D Coded-Aperture Imaging

Early Fusion 3D Image Generation

Development of 3D coded-aperture images based on multi-view data has been one of the key development areas during the first half of fiscal year 2023. To generate such images, we are using maximum likelihood expectation maximization (MLEM) as an early fusion technique that directly projects the unprocessed coded-aperture data onto a voxelated 3D scene. This iterative Bayesian technique takes a current image, $\boldsymbol{I^s}$, and projects it through the system response matrix, $\boldsymbol{M}$, to create a trial detector, $\boldsymbol{D^s}$, and compares it to the data from the imager, $\boldsymbol{d}$, to create a correction matrix that is cast back through the system response matrix to update the image to the next iteration. Specifically, the j^{th} pixel of the next iteration of the image is given by:

$$I_j^{s+1} = \frac{I_j^s}{\sum_{i=1}^{n} M_{ij}} \sum_{i=i}^{n} M_{ij} \frac{d_i}{D_i^s}. \quad (1)$$

Recognizing that

$$D_i^s = \sum_{k=1}^{m} M_{ik} I_k^s, \quad (2)$$

yields the standard form:

$$I_j^{s+1} = \frac{I_j^s}{\sum_{i=1}^{n} M_{ij}} \sum_{i=i}^{n} \frac{M_{ij} d_i}{\sum_{k=1}^{m} M_{ik} I_k^s}. \quad (3)$$

While this expression is well behaved and will converge to a solution, it cannot handle negative numbers. This means that it cannot be applied using the standard mask cross-correlation analysis where the mask function with values of ±1 is used. Instead, a positive-definite system response matrix that correctly scales the counts seen in each detector pixel from a source in any pixel of the image is used. The scale factors must include solid angle and any other location-dependent factors including Poynting vector terms, mask self-collimation, etc. These matrices are generated using the simulation Monte Carlo models discussed below.

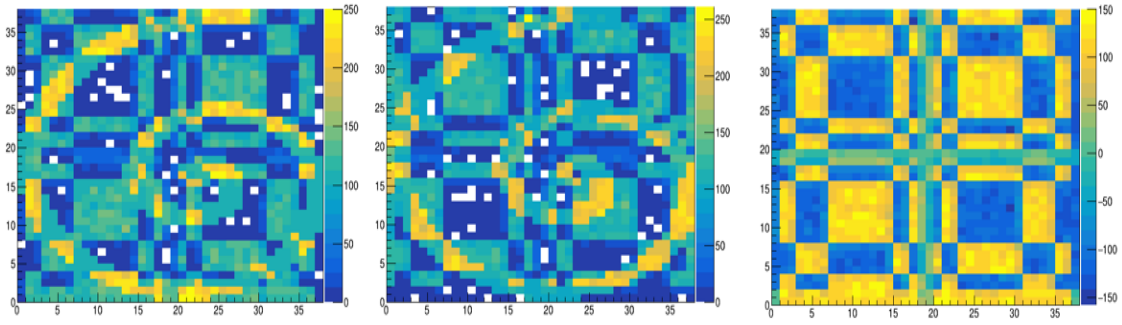

Fig. 1. Simulated data of a point source and a spiral background. In the standard approach the anti-mask data (center) is subtracted from the mask data (left) to remove the background (right), but yields negative detector values.

To handle the mask/anti-mask data collection, which is normally subtracted and generates negative numbers, we follow the work of Brubaker [2], where the system response from a single imager is broken into several components: a mask term, an anti-mask term, and a general background term (Fig. 1). The mask term links each detector pixel to the flux received from a source in each voxel of the image. The coded-aperture data are generally collected in two equal-time integrations, one with the coded-aperture mask and one with its inverse or anti-mask, where the open and closed mask elements are interchanged.[1] This approach is used to handle background reaching the detector, specifically any terms that vary spatially across the detector due to such issues as scatter off of nearby objects and detector nonlinearities can cause artifacts in the image if not removed, and the combined mask/anti-mask data provides a technique to measure and remove them in situ, normally by subtraction. Since subtraction is not allowed by the positivity constraint of the MLEM approach, the system response is expanded to include an anti-mask matrix that is similar to the mask matrix, but with the open and closed pixels interchanged. The detector size is doubled to encompass a “mask” portion and an “anti-mask” portion with each source pixel linked to the mask pixels with the mask matrix and to the anti-mask pixels through the anti-mask matrix (Fig. 2). This separation is possible because the data are time-tagged to

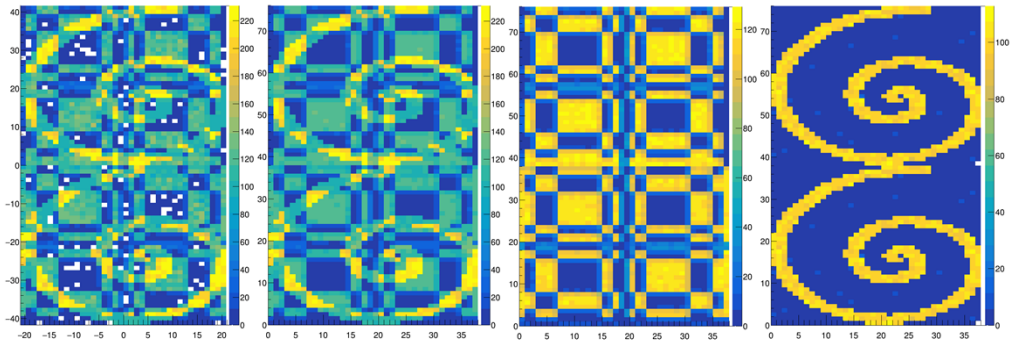

Fig. 2. MLEM approach. The left image is the same simulated data from Fig. 1, but now displayed as a single larger detector with the mask and anti-mask detectors stacked into a single structure. The MLEM detector after fitting (2nd from left), matches the composite detector well, and can be split into terms that include only the coded-aperture-modulated signal (3rd from left) and the background (right).

[1] The mask patterns used in the H420 are anti-symmetric on a 90° rotation, so the exchange is handled autonomously by the imager.

determine when the mask is in its mask and anti-mask orientations. A final component of the response matrix is used to determine general background. This handles uniform background flux that is not modulated by the mask, for instance from a source behind the detector. It will add the same flux to each mask/anti-mask detector pixel pair, regardless of the mask configuration, but can vary across the face of the overall detector.

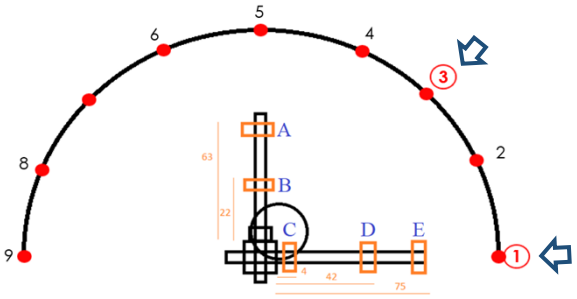

Fig. 3. Measurement setup for comprehensive 3D data. Sources can be placed at any of the labeled orange rectangles (A-E) with data collection locations at a radial distance 1.5 m from the center of the source holder (approximately where the arms cross). The 9 measurement locations cover 180° and are uniformly spaced at 22.5°. The sample MLEM results shown are reconstructed using data from locations 1 and 3 as indicated by the blue arrows.

This approach is being applied to the systematic 3D data collected at the end of the last fiscal year. For that data, an L-shaped source holder with a number of potential source locations was used with various source configurations that were imaged from nine different locations (Fig. 3). At each location a set of contextual data were also collected for generating voxelated maps of the source region. (For the moment we have used the known source holder geometry to voxelate the volume directly.) The MLEM technique is being developed with the different source configurations, initially using only data from a single view angle. More recently, two view angles (see Fig. 3) were used to obtain 3D results (Fig. 4). To incorporate the additional view, the system response matrix is expanded to include the response of each detector pixel of the mask and anti-mask detectors corresponding to each view angle to each voxel of the scene. This approach can easily be scaled to any number of view angles, although the number of detector pixels increases proportionately, increasing the number of steps in each MLEM iteration. We are currently performing the processing using a single desktop computer and take advantage of the graphics card to perform the iteration steps in parallel to reduce the processing time.

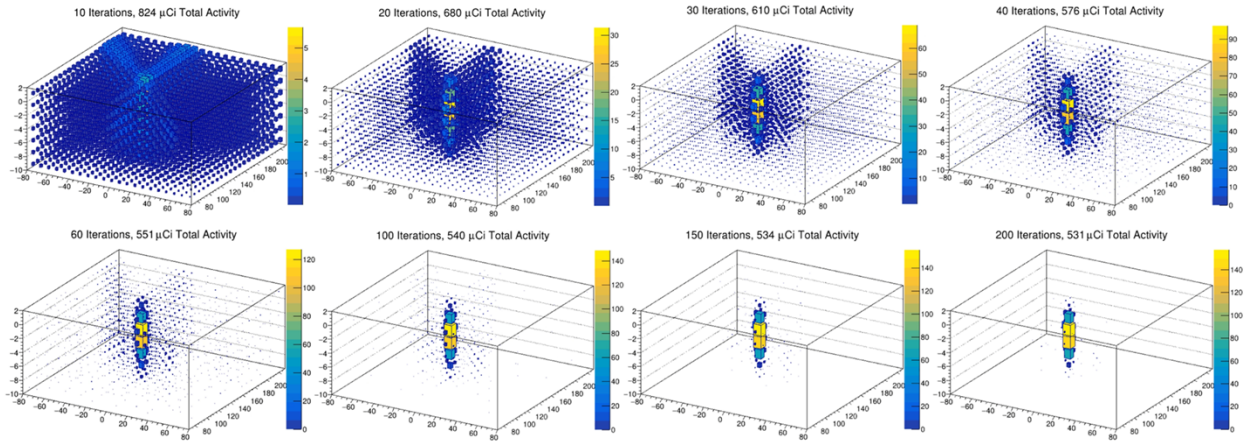

Fig. 4. MLEM reconstruction from two angles of a single point source. From left to right, the upper row shows the images obtained after 10, 20, 30, and 40 iterations. Similarly, the bottom row shows the results after 60, 100, 150, and 200 iterations. The cylindrical nature of the source is an artifact of the exaggerated scale of the z-axis.

One of the advantages of a full contextual data set is that when performing the voxelization, one can identify voxels that contain or are inside closed surfaces. It is only such voxels that can hold source material since we are not concerned with airborne radioisotopes. As such, the MLEM reconstruction is performed including only those locations, reducing the number of voxels that must be included in a reconstruction (Fig. 5).

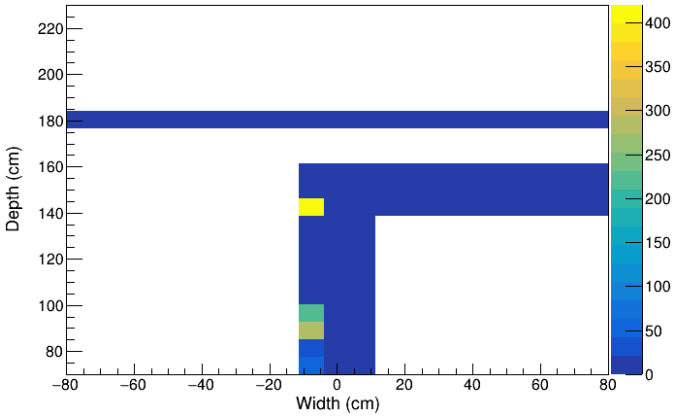

Fig. 5. Top-down view of an MLEM reconstruction of a two-source configuration. In this analysis the algorithm only used source voxel locations that correspond to surfaces. The voxels at depth 180 cm correspond to an artificial back wall added to the voxel map.

While the MLEM results obtained so far are promising, yielding source locations and quantities that are close to those used in the measurements, they are still outside the accuracy we hope to achieve during the project. For the moment, the discrepancies can be attributed to the fact that the system response matrix is based on the results of the Monte Carlo simulations and those remain disappointingly inaccurate when compared to standard analysis techniques as discussed below.

Monte Carlo Simulations

Exploration of the discrepancies between Monte Carlo simulations and measurements of the imager response have continued. Specifically, the imager's coded-aperture response is measured by placing the imager in front of a 2 × 2 m^2, 2-axis, computer-controlled stage (Fig.6). A point source attached to the stage is moved throughout the instrument's field of view and the data analyzed to determine the measured source intensity at each location from a 39 × 39 grid of locations. False color sensitivity maps (Fig. 7) of the data consistently show reduced sensitivity at outer reaches of the scans when compared to Monte Carlo simulations of the same configuration. This is particularly noticeable on the diagonals where a diamond pattern is evident in the data, that is not seen in the simulations.

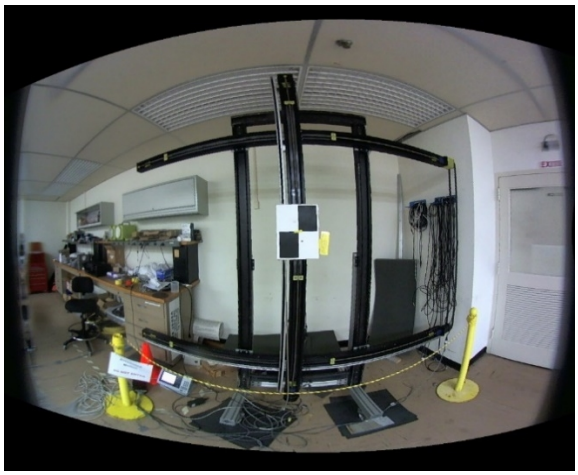

Fig. 6. Visible-light image of the 2 × 2 m^2 translation stage taken by the H420 internal camera.

The simulations are performed in two parts. First, a Geant4 model of the imager is used with a source sequentially located at each of the scan locations. For each such geometry, gamma-ray emissions from the source are simulated and used to determine where gamma-rays deposit energy in the detector. The model includes the mask and major structural elements of the imager based on information obtained from the manufacturer. The energy depositions are then turned into events using a physics model of the detector that includes spatial and spectral response models that approximate those observed with the detector to obtain a list-mode data file that is replayed through the same analysis routines used to analyze data from the detector. It is the result of that analysis that is compared to the detector scan data.

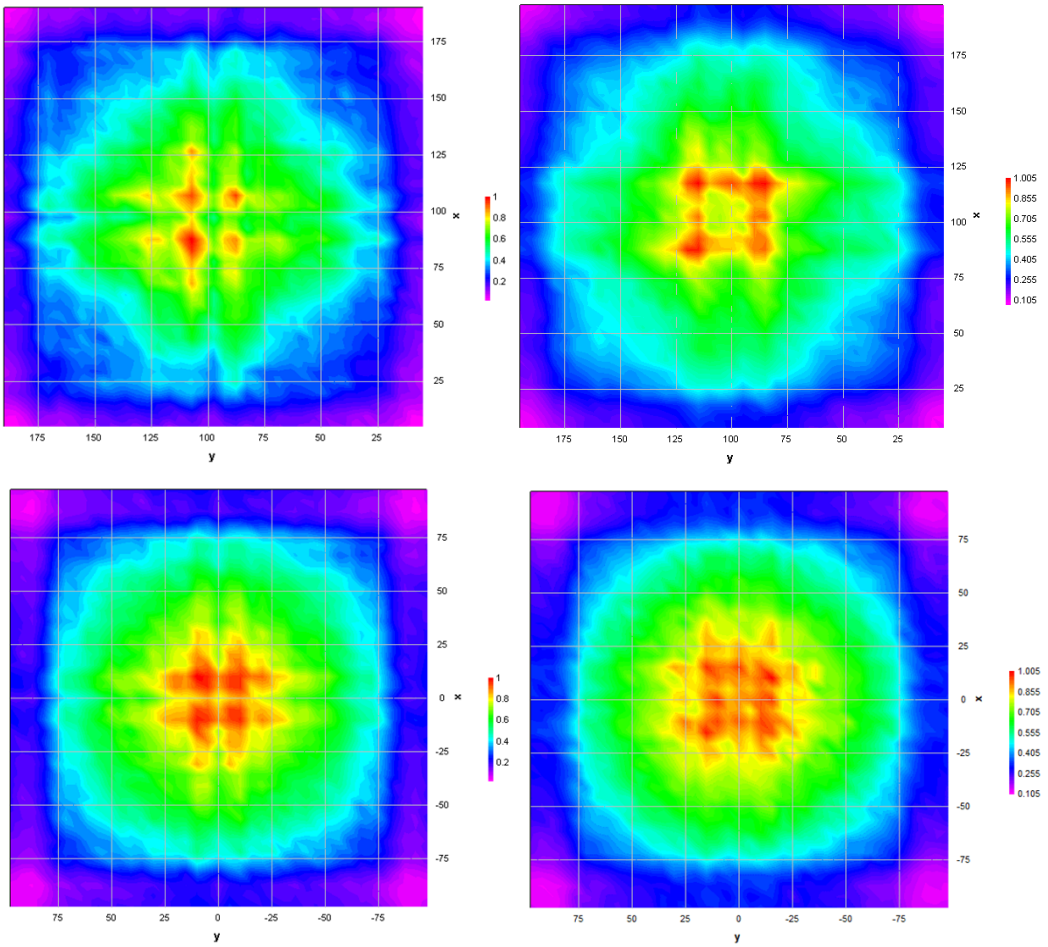

Fig. 7. (Top) False-color sensitivity maps obtained with two different imagers and mask patterns and (bottom) simulated data for the same configurations. While the central sensitivity changes with the mask pattern, the low response in the corners is common between the two.

The source of the discrepancy between the simulations and the detector data can be localized to the detector physics model, by comparing the simulated and measured response map shapes of the total number of counts seen by the detector (Fig. 8), rather than the imaged data. Those results are in good agreement and indicate that the correct number of events are generated in the detector at each

simulated source location. Given that Geant4 is a well validated Monte Carlo code, we expect that the events are not only correct in number, but in the details of where and how much energy is deposited in the detector. This means that the physics models used to turn those depositions into event locations are somehow incorrect, and this makes sense in that the details of where events are recorded impacts the shadowgrams created, and in turn, this impacts the source intensity seen in the imaged data.

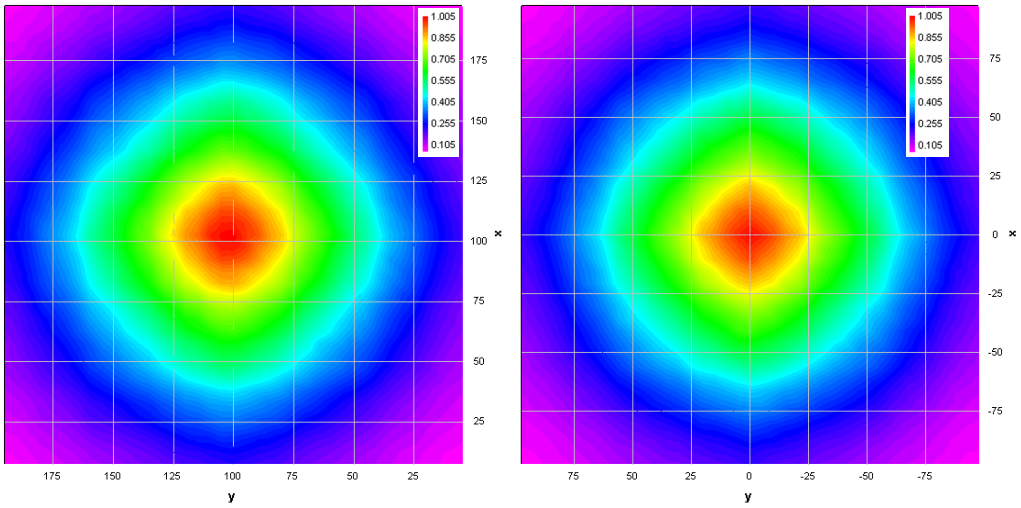

Fig. 8. False color data (left) and simulation (right) maps for the number of events without imaging.

Because the overall diamond pattern was observed with multiple H420 imagers and with different mask versions, it was hoped that there was a common blurring function that could be applied to all of the detectors, e.g., without having to account for small differences between individual imagers. However, over the course of the project a number of blurring schemes have been tried, and the divergence between the simulations and the data have stubbornly remained. We have also looked for unexpected divergence between the model used in the simulations and the actual detector hardware. The last attempt included replacing the standard H3D potted mask with one manufactured from tungsten sheets that had clear openings. While none of these efforts resolved the issue, the mask with clear openings has clear benefits in terms of improved sensitivity at low energies and should be considered for use where weak, low-energy, signals are expected.

The work to improve the spatial physics model has included collecting data with pencil radiation beams to map the detector response directly. This work, reported previously (see annual report for FY 2022), indicated that local event rates could impact the mapping and led to the use of fan beams defined by narrow slits with weaker sources. Even those results indicated some event-rate artifacts might be impacting the results, so we have revisited this work by using multiple narrow slits and local source intensities similar to those used to collect the characterization data (Fig. 9). Unfortunately, general blurring algorithms generated with those data also have not resolved the issue. In the coming quarter, we will use those data to generate detailed, detector-specific responses and see if those resolve the discrepancies.

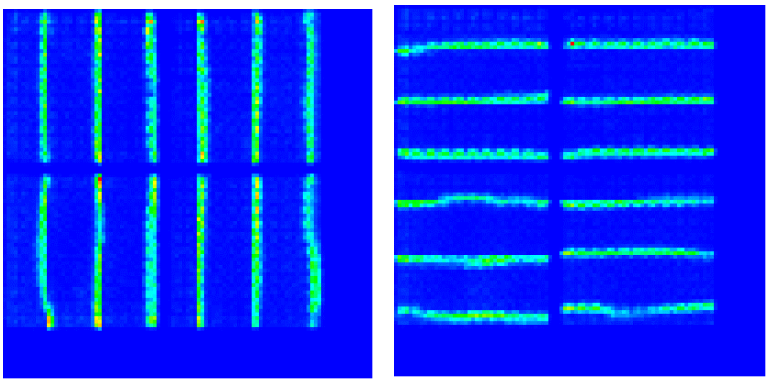

Fig. 9. Slit scan data taken using a ^{57}Co source with one of the imagers. The slits are 500 µm wide with a 6.85 mm pitch.

Conclusions

We are making good progress with implementing the MLEM 3D coded-aperture image reconstruction. Unfortunately, obtaining high quality results will require resolving the simulation issues since we are planning on using those to make the system response matrices. In the near future we plan to explore the limits of the MLEM performance using both simulated data and simulated response matrices so that the data better matches the sytem response. At the same time, we will generate a detailed response model of at least one of the imagers using the multi-slit scan data to see if that improves the conrrespondance between the measured and simulated sensitivity maps.

Publications:

K.P. Ziock, K. Schmitt, J. Daughhetee, A. Ziabari, D. Hellfeld, T.H.Y. Joshi, M. Folsom, S. Brown, D. Goodman, W. Kaye, S. Horne, K. Knecht, D. Gunter, "Nuclear Materials Safeguards with Scene-Data-Fusion-Enabled Gamma-ray Imaging," Proc. of the IAEA Symp. on International Safeguards: Reflecting on the Past and Anticipating the Future, IAEA CN-303,Vienna, Austria, Nov. 2022.

A poster on the progress toward calibrating the H420 imager was presented at the 2022 IEEE Nuclear Science Symposium, as was an oral presentation on the work to find optimum locations to collect data.

References:

1. J.L. Tain, C. Cano-Ott, "Alogrithms for the analysis of B-decay total absorption spectra," *Nucl. Inst. Meth. in Phys. Res.*, **A571**, pp. 728-738, 2007, doi:10.1016/j.nima.2006.10.098.
2. E.M. Brubaker, "A Maximum Likelihood Expectation Maximization Iterative Image Reconstruction Technique for Mask/Anti-mask Coded Aperture Data," Proc. IEEE Nucl. Sci. Symp. and Med. Imaging Conf., 2013.
3. S. Agostinelli et al., "GEANT4—a simulation toolkit," *Nucl. Instr. Meth. in Phys. Res.*, **A506**, pp. 250-303, 2003, doi: 10.1016/S0168-9002(03)01368-8.